

Cohesin and condensin extrude DNA loops in a cell-cycle dependent manner

Stefan Golfier^{1,2,3,4}, Thomas Quail^{1,2,3,4}, Hiroshi Kimura⁵, Jan Brugués^{*1,2,3,4}

Affiliations:

¹Max Planck Institute of Molecular Cell Biology and Genetics, 01307 Dresden, Germany

²Max Planck Institute for the Physics of Complex Systems, 01187 Dresden, Germany

³Centre for Systems Biology Dresden, 01307 Dresden, Germany

⁴Cluster of Excellence Physics of Life, TU Dresden, 01062 Dresden, Germany

⁵Cell Biology Center, Institute of Innovative Research, Tokyo Institute of Technology, 4259 Nagatsuta-cho, Midori-ku, Yokohama 226-8503, Japan

* correspondence: bragues@mpi-cbg.de

Abstract:

Loop extrusion by structural maintenance of chromosomes complexes (SMCs) has been proposed as a mechanism to organize chromatin in interphase and metaphase. However, the requirements for chromatin organization in these cell cycle phases are different, and it is unknown whether loop extrusion dynamics and the complexes that extrude DNA also differ. Here, we used *Xenopus* egg extracts to reconstitute and image loop extrusion of single DNA molecules during the cell cycle. We show that loops form in both metaphase and interphase, but with distinct dynamic properties. Condensin extrudes DNA loops non-symmetrically in metaphase, whereas cohesin extrudes loops symmetrically in interphase. Our data show that loop extrusion is a general mechanism underlying DNA organization, with dynamic and structural properties that are biochemically regulated during the cell cycle.

Introduction:

Chromatin undergoes a dramatic reorganization during the cell cycle¹⁻³. In interphase, chromatin is organized into compartments and topological-associating domains (TADs) that are cell-type specific⁴⁻⁶. TADs are composed of chromatin loops that have been hypothesized to regulate gene expression by spatially restricting contacts between genes and regulatory elements⁷⁻¹⁰. In metaphase, chromosomes undergo large-scale compaction, leading to the loss of specific boundaries and the shutdown of transcription, which is achieved by arranging chromatin into an array of condensed loops¹¹⁻¹⁶. These different degrees of organization require the coordinated activity of protein complexes such as structural maintenance of chromosomes (SMCs) proteins¹⁷⁻²², but how these complexes organize chromatin dynamically during the cell cycle is still unknown. SMCs are thought to organize DNA

by actively extruding DNA loops^{6,19,23,24}. Recent experimental studies have shown that yeast condensin extrudes DNA loops in a one-sided manner *in vitro*²⁵. Although consistent with the loop-extrusion hypothesis, it is inconsistent with the requirement for two-sided loop extrusion predicted by theory^{26,27}. One reason for this discrepancy could be that the properties of loop extrusion in cellular contexts differ from those *in vitro* and may be regulated during the cell cycle^{28,29}. Notably, condensin complexes do not structure the genome during interphase³⁰, which raises intriguing questions about the molecular players that regulate DNA architecture in interphase. Recent *in vitro* work demonstrated that cohesin can extrude DNA loops symmetrically^{31,32}, though this activity has not been directly visualized in cellular contexts^{33–35}. To bridge the gap between *in vitro* biochemical assays and physiological conditions, we used histone H3/H4-depleted *Xenopus laevis* egg extracts to reconstitute loop formation on single DNA molecules. These extracts can be cycled between metaphase and interphase and recapitulate many sub-cellular biological processes, such as the formation of mitotic chromatids and interphase nuclei^{1,36}.

Results:

To visualize DNA loop formation in *Xenopus laevis* egg extracts, we attached lambda-phage DNA to a cover slide using biotin-streptavidin linkers³⁷ in custom-built microfluidic chambers (Fig. 1A). Addition of either metaphase-arrested or interphase *Xenopus* egg extracts into the chamber triggered the formation of small DNA enrichments, consistent with nucleosomal deposition^{38,39}, that rapidly reduced any slack in the DNA molecules (Fig. 1 – Figure supplement 1A and Videos 1-2). To increase the amount of available slack to allow for loop extrusion, we abolished nucleosomal assembly along the strand by depleting ~90-95% of soluble H3-H4 heterodimers in the extract⁴⁰ (Fig. 1 – Figure supplement 1B). This led to the formation of compacted DNA clusters that grew in size over time in both metaphase and interphase (Fig. 1B and Videos 3-8). To investigate whether these clusters exhibited a topology consistent with DNA loops, we hydrodynamically stretched the DNA strand by applying a flow in the perpendicular direction to the strand. This procedure revealed DNA clusters with a characteristic loop topology in both inter- and metaphase extracts (Fig. 1C, Fig. 1 – Figure supplement 1C and Video 9-12). In mock-depleted extracts, loops also formed but at a much lower frequency (Fig. 1 –

Figure supplement 1D and Video 13) and seemed to compete with nucleosomes for available DNA slack. These results show that DNA loop extrusion can be reconstituted in *Xenopus* egg extracts in metaphase and interphase.

To characterize the dynamic properties of loop formation in *Xenopus* egg extracts, we quantified the DNA distribution inside the loop and to the left and right of the loop as a function of time (Fig. 2). We computed the loop extrusion rate from the DNA amount that entered the loop over time, and could determine whether this DNA came from one or both of the non-looped regions. Briefly, we summed the fluorescence intensity of the DNA along the perpendicular direction to the DNA strand, and tracked the loop position defined by the local maximum of the DNA intensity. We then fitted a Gaussian function to the loop region and defined the loop boundaries as ± 2 standard deviations away from the maximum value of the fit (Fig. 2A). We obtained the amount of DNA inside the loop as the difference between the integrated intensity in the loop region minus the offset intensity from the Gaussian fit. Finally, the amount of DNA to the left and right of the loop corresponded to the integrated intensity of the DNA strands outside the loop region (see Supplementary Methods). This assay allows us to observe loop extrusion in extract, to quantify the partitioning of DNA between the looped and non-looped regions, and to examine the symmetry of the underlying DNA extrusion process.

When applied to metaphase-arrested, H3-H4-depleted extract (n=7 extract days), this assay showed that loops are initially extruded at 2.36 ± 0.35 kb/s (mean \pm SEM) (Fig. 2Bi, 2C, and Fig. 2 – Figure supplement 1A). However, loop growth rapidly slowed down as more DNA was pulled into the looped region (Fig. 2 – Figure supplement 2A), suggesting that extrusion rates depend on DNA tension. To examine the relationship between loop extrusion and DNA tension, we used the worm-like chain model⁴¹ that relates the relative extension of the DNA outside the loop to the corresponding force on the DNA strand (see supplementary methods, Fig. 2 – Figure supplement 2 and Fig. 2 – Figure supplement 6). The relative extension outside the loop is a dynamic quantity defined as: $RE(t) = L / (CL_{\lambda} - DNA_{loop}(t))$, where L represents the end-to-end binding distance of the DNA molecule on the coverslip, CL_{λ} is the contour length of lambda-phage DNA, and DNA_{loop} is the amount of DNA in the looped region. These results show that the relationship between extrusion rates

and DNA tension is generally conserved for all looping events (Fig. 2 – Figure supplement 2F). Finally, loop extrusion stopped when the relative extension of DNA outside of the loop reached on average ~65%, corresponding to a stall force of 0.16 pN \pm 0.01 pN (mean \pm SEM), (Fig. 2D). In rare cases, we observed individual looping events stalling at DNA extensions of up to ~85%, corresponding to forces up to ~1 pN (Fig. 2 – Figure supplement 2C-5C).

To characterize the extrusion symmetry in metaphase, we quantified the total decrease in DNA from the left and right regions of the loop between the onset of loop formation and the final steady-state size of the loop (Fig. 2Bii). We used these quantities to define a symmetry score as the relative difference between the decrease of these two regions and the total amount of DNA extruded (supplementary methods). The majority of metaphase looping events had a symmetry score close to 1, which corresponds to one-sided loop extrusion (Fig. 2Biii). However, a small population of ~20% of all metaphase looping events were two-sided (as defined by a symmetry score of less than 0.5, Fig. 2 – Figure supplement 3A). To complement these symmetry score results, we tracked loop movement along the DNA strand (Fig. 2 – Figure supplement 4). Consistent with one-sided loop extrusion, loops that were displaced during loop formation, moved with equal probability towards the boundaries or the center of the strand. This behavior is suggestive of non-symmetric extruding factors landing in a random orientation on the DNA molecule. Taken together, our analysis demonstrates that DNA loop extrusion in metaphase is predominantly one-sided, with extrusion speeds and stall forces similar to those measured *in vitro*^{25,42,43}.

Next, we used interphase H3-H4-depleted extract (n=8 extract days) to investigate whether the dynamics of loop extrusion share similar properties throughout the cell cycle (Fig. 2Civ-vi). Loop extrusion in interphase displayed a similar distribution of extrusion rates, with a mean of 1.94 \pm 0.26 kb/s, and average stall forces of 0.18 pN \pm 0.03 pN, with maximal forces of up to 0.82 pN (Fig. 2C, 2D, Fig. 2 – Figure supplement 2F). However, the distribution of symmetry scores of these looping events peaked towards zero, indicating that these loops are symmetrically extruded. Similar to metaphase looping, we observed that a sub-population of ~20% of all loops had the opposite symmetry (symmetry score larger than 0.5, Fig. 2 – Figure supplement 3B). As predicted for symmetric extrusion, loops that started off-center

on the strand displayed a strong bias to move towards the DNA boundary of the shorter DNA portion (Fig. 2 – Figure supplement 4). Thus, we conclude that the mechanisms of DNA loop extrusion are different in interphase and metaphase.

The different dynamic properties of DNA loop formation that we observe in interphase and metaphase suggest that different molecular activities may be responsible for loop formation during the cell cycle^{5,44}. The cell-cycle-dependent activities of condensin and cohesin could account for the transition between symmetric and non-symmetric loop extrusion^{27,28}. To assess the role of cohesin and condensin during loop extrusion in interphase and metaphase, we selectively depleted these protein complexes in *Xenopus* egg extract. We used custom-made antibodies against XSMC1 and XRad21 for cohesin, and XCAP-C and XCAP-E (SMC2 and SMC4) for simultaneous depletion of condensin I and II (Fig. 3 – Figure supplement 1). We then tested for loop extrusion activity in each depleted condition. We found that, in metaphase (n=3 extract days), the occurrence of loop extrusion was significantly reduced ($p<0.01$) upon depletion of condensin I and II but was unaffected by cohesin depletion (Fig. 3A). In contrast, there was a significant decrease ($p<0.01$) in loop extrusion following cohesin depletion in interphase (n=3 extract days) but was unaffected by condensin depletion (Fig. 3A). We confirmed these depletions with immunostainings that showed colocalization of cohesin and condensin with the loops observed in interphase and metaphase, respectively (Fig. 3B). Additionally, we tested for ATPase activity of the loop extrusion factors by enzymatically depleting ATP using apyrase—which for technical reasons was limited to interphase in extract (see supplementary methods). When applied to interphase extract, apyrase treatment resulted in a near-complete elimination of looping upon ATP depletion, suggesting that cohesin actively extrudes loops in an ATP-dependent manner. Altogether, our results show that cohesin actively extrudes loops symmetrically during interphase, whereas condensin extrudes loops non-symmetrically in metaphase. This demonstrates that the molecular mechanisms of loop extrusion are differentially regulated during the cell cycle.

Discussion:

Our findings provide the first direct evidence that loop extrusion is a general mechanism of DNA organization in a cellular context, and, furthermore, that it is differentially regulated during the cell cycle. This regulation is achieved by the distinct activities of cohesin^{33,34,44} and condensin^{16,21,45} during interphase and metaphase, and may control different levels of DNA organization during the cell cycle: from chromatin that is mostly decondensed and spatially organized into TAD structures during interphase to highly compacted chromosomes in metaphase²⁸. Symmetric loop extrusion by cohesin in interphase may ensure the formation of specific TAD boundaries by bringing together distal CTCF sites^{24,46}. In metaphase, reorganization of loosely packed interphase chromatin into condensed chromosomes leads to the loss of TAD boundaries and the shutdown of transcription^{3,13}, which may be achieved by condensin activity¹⁴. However, many questions remain regarding how the cell cycle regulates condensin and cohesin activities. Previous studies have shown that condensin binds to chromatin in metaphase, but is largely undetected on chromatin in interphase⁴⁷; whereas cohesin is bound to chromatin in interphase, but not as strongly in metaphase^{44,48}. The CDK1-mediated phosphorylation of condensin HEAT subunits in metaphase may be the biochemical signal that triggers the association of condensin to chromatin²¹. In contrast, most cohesin is released from chromatin by a mechanism that involves the phosphorylation of cohesin's SA subunit^{49,50}. Thus, the different affinities of condensin and cohesin for chromatin during the cell cycle could be a natural explanation for the different loop extrusion activities that we see in our experiments.

Our demonstration of predominantly non-symmetric loop extrusion during metaphase is consistent with recent *in vitro* data, but it is at odds with the theoretical requirements to fully compact chromosomes in metaphase^{26,27}. However, these studies suggest that a small fraction of symmetric loop extruders—including extrusion events that reel in DNA at different rates from left and right—can facilitate higher levels of chromosome compaction. Our metaphase data suggest that loops with symmetry scores below 0.8 could be considered “slow” two-sided extrusion events, as DNA is reeled into the loop from both sides, but at different rates. These events account for about 50% of the total population of metaphase looping events, which, according to theoretical predictions, could be sufficient to achieve 100-fold linear chromosome compaction²⁶. Thus, the mixed populations of loop extrusion

symmetries we observe could play a crucial role for proper chromosome organization in metaphase. What is the origin of the small population of symmetric loop extrusion in metaphase? One possibility is that condensin I and condensin II compact DNA using different symmetries⁴³. In *Xenopus* egg extract, the relative abundances of condensin I and condensin II is roughly 5:1⁵¹, which would be consistent with the fraction of nearly symmetric loop extrusion events that we observe in metaphase (~20%). One limitation of our work, however, is that our antibodies simultaneously depleted those two complexes. As a consequence, we cannot rule out that the small population of symmetric loop extrusion may arise from residual cohesin activity in metaphase. In the future it will be interesting to investigate the origin of the different symmetries by using specific antibodies for condensin I and II. In addition, we observe a small sub-population (~20%) of non-symmetric loop extrusion events in interphase, suggesting a differential regulation of extrusion symmetries in both cell cycle phases.

Despite the differences of extrusion symmetries in interphase and metaphase, extrusion rates and stall forces seem to be conserved during the cell cycle. The mean extrusion rates we observe, however, are three to four times higher than those observed in previous *in vitro* studies^{25,32} for cohesin and condensin respectively. One possibility for this discrepancy could be that, in extract, several extruding factors participate in the extrusion of the same DNA loop in a cooperative manner. However, the average stall forces we estimate are about five to seven times lower than previous estimates *in vitro*^{25,32}. We speculate that in cytoplasmic context of the H3-H4-depleted egg extract, many other DNA-binding factors—such as linker histone⁵²—may compete with the loop extrusion machinery for DNA slack. The large spread in the distribution of stall forces, with individual examples reaching values that compare to those reported *in vitro*, may suggest that secondary factors could cause the loop extrusion machinery to stop prematurely, and, consequently, we may underestimate the magnitude of the looping stall forces. We wonder, however, how condensin and cohesin share such similar extrusion rates, even though condensin predominantly extrudes non-symmetrically while cohesin extrudes loops symmetrically. The similar loop growth velocities would suggest that condensin reels in DNA from one side at twice the rate that cohesin reels in DNA from each of its two sides. This assumes, however, that cohesin functions by simultaneously extruding

DNA from two sides. Alternatively, cohesin may be a one-sided motor that alternates its extrusion direction²⁷—though we did not observe switching within the temporal resolution of our measurements. We speculate that symmetric cohesin extrusion could originate from the dimerization of two identical non-symmetric motors, though recent *in vitro* work shows that this idea is controversial^{31,32}. Interestingly, our results comparing extrusion velocities and corresponding symmetries in interphase show that, on average, symmetric loop extrusion rates are higher (roughly twice) compared to the non-symmetric events (Fig. 2 – Figure supplement 5A). This difference in extrusion rates would be consistent with symmetric and non-symmetric loop extrusion mediated by a dimer and a monomer respectively. Our assay will allow for the dissection of the biochemical underpinnings of these processes, and more generally make it possible to reconstitute complex processes such as the formation of boundary elements and the interplay between transcription, replication, and loop extrusion in cellular contexts.

Methods

***Xenopus laevis* egg extract preparation, immunodepletions, and ATP depletion**

Cytostatic factor (CSF)-arrested *Xenopus laevis* (RRID: XEP_Xla_100) egg extract was prepared as described previously³⁶. In brief, unfertilized oocytes were dejellied and crushed by centrifugation, generating an extract that was arrested in meiosis II. We added protease inhibitors (LPC: leupeptin, pepstatin, chymostatin) and cytochalasin D (CyD) to a final concentration of 10 µg/ml each to the extract. In order to generate interphase extracts, CaCl₂ was added to a final concentration of 0.4 mM. To immunodeplete soluble H3-H4 heterodimers from the extract⁴⁰, we coupled 130 µg of a mouse monoclonal anti-H4K12Ac (gift from Hiroshi Kimura) to 12.5 µl rProtein A Sepharose (GE Healthcare) slurry in antibody coupling buffer (10 mM K-HEPES pH=8, 150 mM NaCl), rotating overnight at 4 °C. After several washes with a wash buffer (10 mM HEPES pH=7.7, 100 mM KCl, 150 mM Sucrose, 1 mM MgCl₂), we combined 50 µl fresh CSF extract with the beads and incubated the bead-extract mixture for 1.5 hours on ice, occasionally flicking the tubes in order to prevent the beads settling to the bottom. After recovering the extract from the beads, we

immediately proceeded with the experiment. We generated mock-depleted extracts with the same protocol using 130 µg random mouse IgG antibodies (IgG from Mouse (polyclonal)-unconjugated, Jackson Immuno Research) in 50 µl of fresh CSF extract. To co-deplete H3-H4 and both condensin I and condensin II, we coupled 130 µg anti-H4K12Ac and 10 µg rabbit polyclonal antibodies of both anti-XCAP-C and anti-XCAP-E to 15 µl rProtein A Sepharose slurry and performed the same H3-H4 depletion method. To co-deplete H3-H4 and cohesin, we coupled 130 µg anti-H4K12Ac and 10 µg rabbit polyclonal anti-XRad21 and 10 µg anti-XSMC1 to 15 µl rProtein A Sepharose and performed the same H3-H4 depletion method. ATP was depleted by adding 0.03 U/µl apyrase (A6410; Sigma-Aldrich) to the extract reaction in the presence of 5 mM CaCl₂, followed by a 15 min incubation at room temperature. The ATP-depleted extract was then introduced into the DNA channels as described below.

Western blots

We prepared 1:25 dilutions of immunodepleted extract in 1X sample loading buffer (50 mM Tris-HCl, pH=6.8, 2% SDS, 10% glycerol, 0.006% bromophenol blue, 100 mM DTT), ran a gel electrophoresis on a gradient gel, transferred to a nitrocellulose membrane with a semi-dry transfer approach, and performed primary antibody incubation with polyclonal rabbit antibodies anti-H3 (1:10000, ab1791, RRID: AB_302613), anti-XSMC1 (1:2500, MPI-CBG antibody facility), anti-XCAP-C (1:2000, MPI-CBG antibody facility) and monoclonal mouse antibodies to detect tubulin using anti-DM1a (1:10000, MPI-CBG antibody facility). We detected primary antibodies using LI-COR IRDye secondary antibodies and imaged the western blots using an Odyssey Infrared Imaging System. We analyzed the blots using FIJI.

Antibody production and labeling

We raised rabbit polyclonal antibodies for immunodepletion against peptides SDIVATPGPRFHTV and DLTKYPDANPNPND corresponding to antibodies that targeted cohesin's XRAD21 and XSMC1 subunits. We also raised rabbit polyclonal antibodies against peptides AAKGLAEMQSVG and SKTKERRNRMEVDK corresponding to antibodies that targeted XCAP-C and XCAP-E for both condensin I and II for immunodepletion²¹. We added a cysteine residue on the peptide's N-terminus for sulfhydryl coupling, and subsequent keyhole limpet hemocyanin

conjugation and affinity purification was performed by MPI-CBG antibody facility. We labeled antibodies with fluorophores for localization using the small-scale on-resin labeling technique from⁵³. Briefly, we prepared a 200- μ l pipette tip to act as our resin bed. We then loaded 40 μ l of rProtein A Sepharose (GE Healthcare) resin into the tip, washing three times with 10 mM K-HEPES (pH=7.7), 150 mM NaCl. We labeled both the antibody targeting the cohesin subunit XRad21 and the antibody targeting condensin I and II's subunit XCAP-C. We flowed 70 μ g antibody 5 times consecutively through the packed resin bed in order to bind the antibody to the resin. The resin was then washed three times with 200 mM K-HEPES (pH=7.7). We then added 0.5 μ l 50 mM NHS-Ester-Alexa488 (Alexa FluorTM NHS Ester, A20000, Thermo Fischer) to 25 μ l 200 mM K-HEPES (pH=7.7), and immediately added it to the resin, incubating the resin, antibody, and dye for 10-60 minutes at room temperature. To remove the unbound dye, the resin bed was washed 5 times with 10 mM K-HEPES (pH=7.7), 150 mM NaCl. We eluted the labelled antibody with 5x15 μ l of 200 mM acetic acid. We neutralized each eluate immediately with 5 μ l of 1 M Tris-HCl, pH=9, and cooled to 0 °C. The labelled antibody is stable for months kept at 4 °C.

DNA functionalization

To biotinylate DNA purified from lambda-phage (λ -DNA)⁵⁴, we combined 10 μ g of λ -DNA (NEB, N3011S) and 5 μ l of a 10X polymerase buffer (50 mM Tris-HCl, pH=7.2, 10 mM MgSO₄, 100 μ M DTT) to a total reaction volume of 50 μ l. We then heated the mixture up to 65 °C for 7 minutes to break apart the λ -DNA's sticky ends. After heat treatment, we added 100x molar excess of biotinylated dATP, biotinylated dUTP, and dGTP, and dCTP. We then added 1 unit (~1 μ l) of Klenow enzyme, mixed well, and incubated overnight at room temperature. We purified the biotinylated λ -DNA using ethanol precipitation and stored at -20 °C.

PEGylation of cover slips and DNA micro-channel preparation

We functionalized glass cover slips with mPEG and PEG-Biotin. Briefly, we sonicated coverslips first in acetone for 15 minutes followed by 5 rinses with MilliQ water, and then another sonication step in 5 M KOH for 40 minutes. After rinsing the coverslips 3 times with water and then 3 times with methanol, we dried the coverslips with N₂. We silanized the coverslips combining 250 ml methanol, 12.5 ml acetic acid, and 2.5 ml (3-aminopropyl)-trimethoxysilane, incubating the coverslips in this mixture for 10

minutes at room temperature, sonicating for 1 minute, and then incubating the coverslips for an additional 10 minutes. Next, we rinsed the coverslips once with methanol, once with water, and once again methanol, and dried with N₂. Then we mixed 100 mg mPEG and ~1.5 mg Biotin-PEG with 450 µl PEGylation buffer (0.1M Sodium Bicarbonate, pH=8.5), and spun the reaction at 10000 RPM for 1 minute to remove air bubbles. We pipetted 25 µl of the PEG mixture onto a dried, silanized coverslip and put another coverslip on top, generating a coverslip sandwich. We incubated these sandwiches over night in distilled water-filled pipette tip-boxes in the dark. After incubation, we carefully disassembled the coverslips, rinsed with MilliQ water, and dried with N₂. To generate a channel for imaging, we first drilled holes through a cleaned cover slide—these holes acted as channel inlets and outlets. We placed custom-designed, laser-cut double-sided tape onto the coverslip, defining the channel geometry. We then placed a functionalized PEG-biotinylated coverslip on top of the double-sided tape, sealing the channel on either end with Valap. We filled the channel with ~10-15 µl of 0.1 mg/ml free streptavidin, incubating the channel with streptavidin for 1 minute. To remove the free, unbound streptavidin, we flushed ~100 µl channel washing buffer (40 mM Tris-HCl, pH=8.0, 20 mM NaCl, 0.4 mM EDTA) through the channel, using the drilled holes as channel inlets and outlets. We added 20 µl of 1:1000 biotinylated λ-DNA (~5 pM), incubating it for ~1 min and then washed the channel with 3x100 µl of channel washing buffer.

Imaging

For live imaging of looping events, we fluorescently stained immobilized DNA strands with 50-500nM Sytox Orange (S11368, ThermoFisher), a DNA intercalating dye, in imaging buffer (50mM Tris-HCl pH 7.7, 50mM KCl, 2.5mM MgCl₂, 2mM ATP) similar to²⁵ or Xenopus Buffer (XB: 100mM KCl, 1mM MgCl₂, 0.1mM CaCl₂, 2mM ATP). We excited Sytox Orange-labelled DNA using a 561 nm laser, and imaged the strands using a Nikon Eclipse microscope stand with a Nikon 100x/NA 1.49 oil SR Apo TIRF and an Andor iXon3 EMCCD camera using a frame-rate of 100 – 300ms. A highly inclined and laminated optical sheet (HILO) microscopy mode was established using a Nikon Ti-TIRF-E unit mounted onto the microscope stand to improve signal-to-noise ratio by excluding background fluorescence signal from unbound DNA dye in the buffer. To trigger the formation of DNA loops, we flowed about 2 ul of H3-H4-depleted extract into the channel (total channel volume ~10ul) and let the extract

diffuse further down the channel. We then imaged looping events at the moving front of the diffusing extract. A typical field of view contained 5 - 20 individual DNA molecules with typically between 2 - 7 strands having sufficient slack to support loop extrusion. Of these about 30% displayed looping events (Fig. 3). As we could not control the concentration of loop extrusion factors, the majority of looping events displayed competition between two loops on the same strand. For this study we selected DNA strands that contained only a single looping event per strand.

Hydrodynamic stretching of loops

To visualize DNA loop topology which cannot be observed in the normal mode of data acquisition, we hydrodynamically stretched DNA strands that exhibited looping events using a flow-controlled syringe pump (Pro Sense B.V., NE-501), see also Videos 9-12. The flow direction was set to be perpendicular to the strand orientation by a cross-shaped channel design. Depending on the width of the channel, we used flow rates between 100 $\mu\text{l}/\text{min}$ and 500 $\mu\text{l}/\text{min}$ to extend DNA loops. Specifically, we introduced H3-H4-depleted extract into the channel as described above and, upon loop formation, stretched DNA strands by flowing imaging buffer from the opposite side.

Correction of dye-induced DNA lengthening

As mentioned above, we used the DNA intercalating dye Sytox Orange at a range of concentrations to visualize our immobilized lambda DNA molecules. The intercalation of small dye molecules in between adjacent base pairs leads to a dye-concentration-dependent lengthening of the DNA molecules' contour length³⁷. As this effect influences downstream analysis, we sought to correct for the dye-induced lengthening of our DNA molecules by determining the effective contour length of the lambda DNA for each dye concentration used in this study. To this end, we hydrodynamically stretched immobilized DNA molecules in the absence of dye using a buffer flow perpendicular to the strand orientation. DNA molecules were visualized by previous covalently labelling of the DNA backbone with Cy5 fluorescent molecules (label IT nucleic acid labelling kit, Mirus) which does not compromise the DNA contour length. By measuring the extension of these DNA molecules at a certain flow rate, we calculated the corresponding force experienced by the DNA molecules using

the worm-like chain model⁴¹. We then performed the same stretching experiment with DNA molecules exposed to various concentrations of Sytox Orange, keeping the flow rate (and thus the stretching force) constant (1.54 pN) (Fig. 2 – Figure supplement 6A). The application of the worm-like chain model to the mean measured DNA extension values for a known force allowed us finally to obtain the contour length of lambda DNA at all examined dye concentrations (Fig. 2 – Figure supplement 6B). All these calibrations were done in the same buffer that is present in the channels prior to introduction of the egg extract—which matches the pH and salt concentration of the extract. However, we want to point out, that in the extract, DNA molecules are exposed to a multitude of DNA binding proteins, which may further influence the properties of the DNA. However, for technical reasons, our calibrations of the effect of the dye on DNA length were limited to the buffer condition.

Loop extrusion analysis

DNA traces were analyzed using custom-written Python scripts motivated by ²⁵, resulting in data files for further analysis that we added together with the source code in the supplement. We converted movies of fluorescent DNA molecules into one-dimensional intensity profiles by summing the intensity values along the direction perpendicular to the DNA strand in each frame. We removed the background signal using a median filter. From the summed intensity profile for each frame we built kymographs by concatenating all time points (Fig. 2 and Fig. 1 – Figure supplement 1). To yield the amount of DNA inside and outside the loop for each time point, we segmented the DNA intensity profiles into a loop region and two regions outside of the loop by first finding the maximum intensity value as the position of the loop and subsequent fitting of a Gaussian around that position. We defined the boundaries of the loop region and the regions outside of the loop by the positions $\pm 2 \times$ standard deviations from the center of the Gaussian fit. Summing the intensity values of the regions outside of the loop and integrating the intensity under the Gaussian fit yielded the proportions of total signal intensity in each of the three regions for each time point. The difference between the integrated intensity below the loop and the offset from the Gaussian fit (corresponding to the intensity outside of the loop) was equally distributed to the regions outside of the loop as the signal from the incoming and outgoing DNA strands that are not part of the loop itself (Fig. 2A).

We calculated the relative sizes of the three regions in kilo-base pairs (kb) for each time frame by multiplying the 48.5 kb total length of lambda DNA with the ratio of each summed intensity value and the total summed intensity of the strand for every time point. From these values we calculated the relative change in each region over time by subtracting the averaged ten last data points from the averaged ten first data points in each region. We used the resulting values *a* and *b* for the region left and right of the loop to assign a symmetry score for each looping event by calculating

$$\text{symmetry score} = \frac{\text{Max}(a, b) - \text{Min}(a, b)}{a + b}$$

This procedure orders the extrusion from region *a* and *b* such that the symmetry score is always positive and ranges from 0 to 1. Our symmetry score intends to quantify the amount of DNA extruded into the loop from the outer regions. A positive relative change from one side implies that no DNA from that side has been extruded into the loop—and indicates that DNA slipped from the loop to that region—, and thus we set that change to 0 (if *a* >0: *a*=0; if *b* >0: *b*=0). The slipping of substantial amounts of DNA (>2kb) was a rare event with 3 cases in metaphase (*p*=0.08) and 0 cases in interphase.

This procedure additionally allowed us to track the position of the loop for each time point during every loop extrusion event and study the movement of loops along the DNA strands in inter- and metaphase (Fig. 2 – Figure supplement 4). To this end we quantified the change in relative position of the loop by subtracting the average loop positions of the last ten time point from the average loop positions of the first ten time points. (Fig. 2 – Figure supplement 4C) This analysis is set up in such a way that, independent of a loop starting left or right of the center of the DNA, the change in loop position will always be positive if the loop moves towards or crosses the center of the DNA molecule, and negative if the loop moves towards the closest DNA boundary. The absolute quantity of the change in loop position reflects the relative displacement of the loop along the DNA strand during the process of loop formation and it is referred to as static, if the displacement is below a threshold of 0.08. This analysis allowed us to display the relative displacements of loops as a function of the symmetry score of the corresponding looping in between meta- and interphase (Fig. 2 – Figure supplement 4D&E) and compare the probability of the loop to move

towards the center of the strand between both cell cycle phases (Fig. 2 – Figure supplement 4F)

We extracted the initial loop extrusion rates from the first derivative at time point zero of a single exponential fit to the values of the loop growth over time (Fig. 2B-C). The size of the loop at each time point further allowed us to continuously calculate the relative extension of the DNA molecule during the loop formation, by dividing the end-to-end distance of the DNA strand by the length of the regions outside of the loop. We estimated the tension on the DNA strand for each time point by applying the Worm Like Chain Model (WLC) of DNA⁴¹ to these relative extension values (Fig. 2 – Figure supplement 2C & D). Since small fluctuations in the estimated relative extension of the DNA, as they occur via thermal agitation of the molecule, can lead to large fluctuations in the corresponding tension, we decided to reduce fluctuations by smoothing the initial loop data. To this end we applied a Savitzky-Golay filter with a 2nd order polynomial and a window size of 63 points to the initial loop data, which significantly reduced fluctuations in the resulting relative DNA extension. The rate of loop extrusion was then extracted from a first order derivative of the smoothed curve and yielded similar initial rates as determined from the exponential fit to the raw loop data. We then applied the WLC model to the smoothed relative extension curve to obtain tension of the DNA molecule for each time point during the loop formation. This procedure allowed us to visualize the decrease in extrusion rate with the increasing tension on the DNA molecule (Fig. 2 – Figure supplement 2E). To investigate the dependence of the rate of loop extrusion on the tension on the DNA strand for the entire population of inter- and metaphase looping events, we extracted the extrusion rates and corresponding tension values for each time point during every looping event from the exponential fits to the loop data. This allowed us to display the average decrease in extrusion rate (+/- standard deviation) for the interphase and metaphase looping populations (Fig. 2 – Figure supplement 2F). The stall force of each loop extrusion event (Fig. 2D) was determined by taking the average steady state loop size of the last ten time points and converting the corresponding relative extension of the DNA molecule into one tension value per looping event using the WLC model. For the analysis of extrusion stall forces we only used DNA strands where the loop extrusion did not end (or was stalled) at the DNA end-binding sites (N = 52).

To quantify the effect of cohesin and condensin depletion, we determined the probability of loop extrusion by counting the number of observable loop extrusion events in all data taken for one condition and dividing it by the total number of DNA strands with sufficient slack ($< 70\%$ relative extension) to support the formation of a loop for that condition.

Acknowledgements

We acknowledge L. Mirny for initial discussions of this work, and A.A. Hyman, P. Tomancak, M. Loose, K. Ishihara, I. Patten, M. Sarov, J. Guck, F. Stewart, F. Jülicher, M. Srinivasan, and K. Nasmyth for discussions and revision of the manuscript. We thank M. Elsner and V. Murugesan for assistance in some of the experiments. We thank H. Andreas for frog maintenance, the Light Microscopy Facility (LMF), and the Antibody Facility at MPI-CBG.

References

1. Hirano, T. & Mitchison, T. J. Cell cycle control of higher-order chromatin assembly around naked DNA in vitro. *J. Cell Biol.* **115**, 1479–1489 (1991).
2. Rowley, M. J. & Corces, V. G. Organizational principles of 3D genome architecture. *Nat. Rev. Genet.* **19**, 789–800 (2018).
3. Nagano, T. *et al.* Cell-cycle dynamics of chromosomal organization at single-cell resolution. *Nature* **547**, 61–67 (2017).
4. Bonev, B. & Cavalli, G. Organization and function of the 3D genome. *Nat. Rev. Genet.* **17**, 661–678 (2016).
5. Dekker, J. & Mirny, L. The 3D Genome as Moderator of Chromosomal Communication. *Cell* **164**, 1110–1121 (2016).
6. Rao, S. S. P. *et al.* A 3D map of the human genome at kilobase resolution reveals principles of chromatin looping. *Cell* **159**, 1665–1680 (2014).
7. Smith, E. M., Lajoie, B. R., Jain, G. & Dekker, J. Invariant TAD Boundaries Constrain Cell-Type-Specific Looping Interactions between Promoters and Distal Elements around the CFTR Locus. *Am. J. Hum. Genet.* **98**, 185–201 (2016).
8. Lupiáñez, D. G. *et al.* Disruptions of topological chromatin domains cause pathogenic rewiring of gene-enhancer interactions. *Cell* **161**, 1012–1025 (2015).
9. Ren, G. *et al.* CTCF-Mediated Enhancer-Promoter Interaction Is a Critical Regulator of Cell-to-Cell Variation of Gene Expression. *Mol. Cell* **67**, 1049–1058 (2017).
10. Schoenfelder, S. & Fraser, P. Long-range enhancer-promoter contacts in gene expression control. *Nat. Rev. Genet.* **20**, 437–455 (2019).
11. Marsden, M. P. F. & Laemmli, U. K. Metaphase chromosome structure: Evidence for a radial loop model. *Cell* **17**, 849–858 (1979).
12. Earnshaw, W. C. & Laemmli, U. K. Architecture of metaphase chromosomes and chromosome scaffolds. *J. Cell Biol.* **96**, 84–93 (1983).
13. Natalia Naumova, Maxim Imakaev, Geoffrey Fudenberg, Ye Zhan, Bryan R. Lajoie, Leonid A. Mirny, J. D. Organization of the Mitotic Chromosome. *Science* **342**, 948–953

(2013).

14. Goloborodko, A., Imakaev, M.V., Marko, J.F. & Mirny, L. Compaction and segregation of sister chromatids via active loop extrusion. *Elife* (2016).
15. Uhlmann, F. SMC complexes: from DNA to chromosomes. *Nat. Rev. Mol. Cell Biol.* **17**, (2016).
16. Kinoshita, K. & Hirano, T. Dynamic organization of mitotic chromosomes. *Curr. Opin. Cell Biol.* **46**, 46–53 (2017).
17. Nasmyth, K. Disseminating the genome: Joining , Resolving , and Separating Sister Chromatids During Mitosis and Meiosis. *Annu. Rev. Genetics* **35**, 673–745 (2001).
18. Yatskevich, S., Rhodes, J. & Nasmyth, K. Organization of Chromosomal DNA by SMC Complexes. *Annu. Rev. Genet.* **53**, 1–38 (2019).
19. Fudenberg, G. *et al.* Formation of Chromosomal Domains by Loop Extrusion. *CellReports* **15**, 2038–2049 (2016).
20. Nuebler, J., Fudenberg, G., Imakaev, M., Abdennur, N. & Mirny, L. A. Chromatin organization by an interplay of loop extrusion and compartmental segregation. *Proc. Natl. Acad. Sci. U. S. A.* **115**, E6697–E6706 (2018).
21. Hirano, T., Kobayashi, R. & Hirano, M. Condensins , Chromosome Condensation Protein Complexes Containing XCAP-C , XCAP-E and a Xenopus Homolog of the Drosophila Barren Protein. *Cell* **89**, 511–521 (1997).
22. Bouwman, B. A. M. & de Laat, W. Getting the genome in shape: The formation of loops, domains and compartments. *Genome Biol.* **16**, 1–9 (2015).
23. Alipour, E. & Marko, J. F. Self-organization of domain structures by DNA-loop-extruding enzymes. *Nucleic Acids Res.* **40**, 11202–11212 (2012).
24. Sanborn, A. L. *et al.* Chromatin extrusion explains key features of loop and domain formation in wild-type and engineered genomes. *Proc. Natl. Acad. Sci.* **112**, E6456–E6465 (2015).
25. Ganji, M. *et al.* Real-time imaging of DNA loop extrusion by condensin. *Science* **360**, 102-105 (2018).
26. Banigan, E. J. & Mirny, L. A. Limits of chromosome compaction by loop-extruding motors. *bioRxiv* 476424 (2018).
27. Banigan, E. J., Berg, A. A. Van Den, Brandão, H. B. & Marko, J. F. Chromosome organization by one-sided and two-sided loop extrusion. *bioRxiv* 815340 (2019).
28. Abramo, K., Valton, A., Venev, S. V, Ozadam, H. & Fox, A. N. A chromosome folding intermediate at the condensin-to-cohesin transition during telophase. *bioRxiv* 678474 (2019).
29. Losada, A., Hirano, M. & Hirano, T. Identification of Xenopus SMC protein complexes required for sister chromatid cohesion. *Genes Dev.* **12**, 1986–1997 (1998).
30. Abdennur, N. *et al.* Condensin II inactivation in interphase does not affect chromatin folding or gene expression. *bioRxiv* 437459 (2018).
31. Davidson, I. F. *et al.* DNA loop extrusion by human cohesin. *Science* **366**, 1338–1345 (2019).
32. Kim, Y., Shi, Z., Zhang, H., Finkelstein, I. J. & Yu, H. Human cohesin compacts DNA by loop extrusion. *Science* **366**, 1345–1349 (2019).
33. Rao, S. S. P. *et al.* Cohesin Loss Eliminates All Loop Domains. *Cell* **171**, 305-320.e24 (2017).
34. Schwarzer, W. *et al.* Two independent modes of chromatin organization revealed by cohesin removal. *Nature* **551**, 51–56 (2017).
35. Hansen, A. S., Pustova, I., Cattoglio, C., Tjian, R. & Darzacq, X. CTCF and cohesin regulate chromatin loop stability with distinct dynamics. *Elife* **6**, (2017).
36. Murray, A. W. Cell cycle extracts. in *Methods in cell biology* **36**, 581–605 (1991).
37. Ganji, M., Kim, S. H., Van Der Torre, J., Abbondanzieri, E. & Dekker, C. Intercalation-based single-molecule fluorescence assay to study DNA supercoil dynamics. *Nano Lett.* **16**, 4699–4707 (2016).
38. Yan, J. *et al.* Micromanipulation Studies of Chromatin Fibers in Xenopus Egg Extracts Reveal ATP-dependent Chromatin Assembly Dynamics. *Mol. Biol. Cell* **18**, 464–474 (2007).

39. Gruszka, D. T., Xie, S., Kimura, H. & Yardimci, H. Single-molecule imaging reveals control of parental histone recycling by free histones during DNA replication. *bioRxiv* 789578 (2019).
40. Zierhut, C., Jenness, C., Kimura, H. & Funabiki, H. Nucleosomal regulation of chromatin composition and nuclear assembly revealed by histone depletion. *Nat. Struct. Mol. Biol.* **21**, 617–622 (2014).
41. Marko, J. F. & Siggia, E. D. Stretching DNA. *Macromolecules* **28**, 8759–8770 (1995).
42. Terence R. Strick, Tatsuhiko Kawaguchi, T. H. Real-time detection of single-molecule DNA compaction by condensin I. *Curr. Biol.* **128**, 189–190 (2004).
43. Muwen Kong, Erin Cutts, Dongqing Pan, Fabienne Beuron, Thangavelu Kaliyappan, Chaoyou Xue, Ed Morris, Andrea Musacchio, Alessandro Vannini, E. C. & Greene. Human condensin I and II drive extensive ATP – dependent compaction of nucleosome – bound DNA. *bioRxiv* 683540 (2019).
44. Losada, A., Hirano, M. & Hirano, T. Identification of *Xenopus* SMC protein complexes required for sister chromatid cohesion. *Genes Dev.* **12**, 1986–1997 (1998).
45. Keishi Shintomi, Fukashi Inoue, Hiroshi Watanabe, Keita Ohsumi, Miho Ohsugi, T. H. Mitotic chromosome assembly despite nucleosome depletion in *Xenopus* egg extracts. *Science* **356**, 1284–1287 (2017).
46. Tang, Z. *et al.* CTCF-Mediated Human 3D Genome Architecture Reveals Chromatin Topology for Transcription. *Cell* **163**, 1611–1627 (2015).
47. Hirano, T. & Mitchison, T. J. A Heterodimeric Coiled-Coil Protein Required for Mitotic Chromosome Condensation In Vitro. *Cell* **79**, 449–458 (1994).
48. Sumara, I., Vorlaufer, E., Gieffers, C., Peters, B. H. & Peters, J. M. Characterization of vertebrate cohesin complexes and their regulation in prophase. *J. Cell Biol.* **151**, 749–761 (2000).
49. Losada, A. & Hirano, T. Shaping the metaphase chromosome: Coordination of cohesion and condensation. *BioEssays* **23**, 924–935 (2001).
50. Hauf, S. *et al.* Dissociation of cohesin from chromosome arms and loss of arm cohesion during early mitosis depends on phosphorylation of SA2. *PLoS Biol.* **3**, 0419–0432 (2005).
51. Ono, T. *et al.* Differential contributions of condensin I and condensin II to mitotic chromosome architecture in vertebrate cells. *Cell* **115**, 109–121 (2003).
52. Xiao, B., Freedman, B. S., Miller, K. E., Heald, R. & Marko, J. F. Histone H1 compacts DNA under force and during chromatin assembly. *Mol. Biol. Cell* **23**, 4864–4871 (2012).
53. Groen, A. C., Nguyen, P. A., Field, C. M., Ishihara, K. & Mitchison, T. J. Glycogen-supplemented mitotic cytosol for analyzing *Xenopus* egg microtubule organization. in *Methods in enzymology* **540**, 417–433 (2014).
54. Smith, S. B., Cui, Y. & Bustamante, C. Overstretching B-DNA: the elastic response of individual double-stranded and single-stranded DNA molecules. *Science* **271**, 795–799 (1996).

Figure 1: Single DNA molecule assay for direct visualization of DNA looping in *Xenopus* egg extracts. (A) (i) Side and top view schematics of a single strand of λ -phage DNA attached to a functionalized cover slip via biotin-streptavidin linkers. (ii) *Xenopus* egg extract is flowed into the microfluidic chamber. (iii) Side and top view schematics visualizing how soluble active loop-extruding factors extrude loops in H3-H4-depleted extract. (B) Dynamics of the formation of DNA loops induced by H3-H4-depleted extract in metaphase (upper) and interphase (lower). Snapshot of a single molecule of λ -phage DNA visualized using Sytox Orange preceding treatment with H3-H4-depleted extract (left). Kymograph of DNA signal over time displaying a looping event upon addition of H3-H4-depleted extract (middle). Snapshot of steady-state DNA looping event after ~60 sec (right). (C) Hydrodynamic flows reveal loop topology within DNA cluster. (i) Schematic of the loop

topology revealed upon flow. (ii) Topology of extract-induced DNA loops in metaphase (upper) and interphase (lower) visualized using Sytox Orange revealed upon flow in the direction of the arrow.

Figure 2: Symmetry of loop extrusion is cell-cycle dependent with similar extrusion rates and stalling forces.

(A) Method to track DNA-loop dynamics through space and time. *Upper:* Schematic of the top view of a DNA-looping event segmented into three regions: region I (orange), region II (green), and the loop region (blue). *Middle:* Snapshot of DNA-looping event where DNA is labelled using Sytox Orange. *Bottom:* The integrated fluorescence intensity of the DNA generated by summing the intensity values along the perpendicular axis of the strand. The dashed red line represents a Gaussian fit to the data. Signal values above the fit's offset define the looped region given in blue; signal values below this threshold correspond to the non-looped regions I and II, given in orange and in green. To convert the signal into DNA length, the integrated intensity of each region is divided by the total summed intensity of the DNA strand and multiplied by the total length of λ -phage DNA (48.5 kb). (B) Dynamics of DNA looping in H3-H4-depleted extract in metaphase and interphase. (Bi,iv left) DNA amount as a function of time computed for the looped region (blue) and non-looped regions I and II (green and orange). The dots represent experimental data and the solid lines represent exponential fits to the data. (Bi,iv right) The redistribution of DNA during the looping events shown in the left panel quantified as the change in DNA content in each region. (Bii, v) Change in the amount of DNA in the looped region and non-loop regions I and II (as in Bi,iv right) for the entire population of meta- and interphase looping events plotted as a function of the initial relative DNA extension of the corresponding molecules. Error bars correspond to standard deviations of data clustered by proximity. Points represent raw data. (Biii, vi) Analysis of loop extrusion symmetry shows predominantly non-symmetric extrusion (symmetry score ~ 1) in metaphase (Biii) and symmetric extrusion (symmetry score ~ 0) in interphase (Bvi). (C) Initial growth rates of DNA loop extrusion in metaphase (red) and interphase (blue) as a function of initial relative DNA extension. These rates were obtained from the slopes of the exponential fits to the loop data at time $t=0$ for the subset of loop extrusion events that allowed for a fitting that converged within a tolerance (10^{-8}) relative change of the cost function), that corresponded to $N=21$ out of 30 in interphase, and $N=24$ out of 34 for metaphase. Error bars were obtained from error propagation of the uncertainties of the exponential fit parameters. (D) Box plots of the stall forces for DNA loop extrusion in metaphase and interphase obtained from the final relative extension of the DNA strand at the end of loop formation.

Figure 3: Condensin extrudes DNA loops in metaphase and cohesin extrudes loops in interphase.

(A) Loop extrusion probability—the frequency at which looping occurs on a strand with sufficient slack—in metaphase and interphase under different depletion conditions. In metaphase, co-depleting condensin I, condensin II, and H3-H4 (using anti-XCAP-C/E and anti-H4K12Ac) significantly (** represents $p<0.01$, Binomial test) reduced loop extrusion probability, whereas the same depletion condition in interphase had no effect on loop extrusion probability compared to H3-H4-depleted extract. However, depleting cohesin and H3-H4 (using anti-XRAD21/XSMC1 and anti-H4K12Ac) had no effect in metaphase, though significantly ($p<0.01$) decreased loop extrusion probability in interphase compared to H3-H4-depleted extract. (B) Snapshots of antibody stainings of representative loops in metaphase and interphase. (Top) In metaphase, Alexa488-labeled anti-XRad21 bound to cohesin does not localize to the loop, whereas in interphase (right panels), the anti-XRad21 co-localizes to the loop. (Bottom) Alexa488-labeled anti-XCAP-C bound to condensin localizes to the loop in metaphase, but does not localize to the loop in interphase.

Supplementary Figure captions

Figure 1 - supplementary Figure 1: Characterization of DNA compaction in *Xenopus laevis* egg extracts. (A) Addition of crude extract to λ -phage DNA molecules leads to the generation of multiple highly-enriched DNA clusters, suggestive of nucleosomal formation along the strand. Alexa488-labeled anti-H3 and anti-H4k12ac localize to these DNA clusters (left). Kymographs of nucleosomal cluster formation in both metaphase (upper) and interphase (lower) along a strand upon addition of crude extract. See also Video 1 and 2. (B) Quantitative western blot showing approximately 90-95% depletion of soluble H3-H4 heterodimers. (C) Examples of completely stretched loops in metaphase (left & middle) and a partially extended interphase loop (right) upon hydrodynamic stretching with buffer flow perpendicular to strand orientation. (D) Kymograph of a looping event on a strand upon treatment with crude extract. See also Video 13.

Figure 2 - supplementary Figure 1: DNA looping examples demonstrating non-symmetric loop extrusion in metaphase and symmetric loop extrusion in interphase. We tracked the position of the loop and segmented the DNA signal into a loop region (blue) and region I and II (orange and green). The integrated fluorescence intensity in each region was converted into the relative amount of DNA in that region as described above and plotted as a function of time. The dots are data from the analysis and the lines represent single exponential fits to the data. (A) In metaphase, we observed a saturating exponential increase in the DNA amount in the looped region, and only a single non-looped region decreasing in DNA amount, suggestive of non-symmetric loop extrusion. (B) In interphase, we observed a similar saturating exponential increase in the DNA amount in the looped region, whereas both non-loop regions decreased in DNA amount, suggestive of symmetric loop extrusion. (C) Representative snapshots of DNA looping in H3-H4-depleted interphase and metaphase extracts ordered by end-to-end distance. Left image represents the initial DNA configuration and right image the corresponding final loop configuration. Scale bar is 5 μ m.

Figure 2- supplementary Figure 2: Biophysical characterization of loop extrusion rate and DNA tension. (A) Example of one metaphase loop extrusion event (blue dots) smoothed by a Savitzky-Golay filtering with a 2nd-order polynomial and a window size of 63 points (black dashes). (B) The extrusion rate of the looping event was obtained from the first-order derivative of the smoothed curve. (C) Relative DNA extension was calculated as the end-to-end distance divided by the amount of DNA outside of the loop region using the raw loop data (blue shaded curve) and the smoothed loop data from (A). (D) Tension on the DNA strand resulting from the reeling of DNA into the loop was obtained from applying the worm like chain model⁴¹ for DNA to the relative extension values in (C) with the raw data as the shaded curve. (E) Rate of loop extrusion plotted over the tension on the DNA strand for the single looping event in (A). (F) Loop extrusion rates over DNA tension for the population of metaphase (blue dots and envelope) and interphase looping events (green dots and envelope) from exponential fit curves to the loop data. Dots represent mean values, error bars and envelope represent standard deviation.

Figure 2- supplementary Figure 3: Examples of symmetric DNA loop extrusion in metaphase and non-symmetric loop extrusion in interphase. We quantified the amount of DNA inside the loop (blue dots) and the regions left and right of the loop (region I in orange and region II in green) from the relative integrated DNA fluorescence intensities in each region for each time point. The lines represent exponential fits to the data. (A) Examples of metaphase looping events exhibiting symmetric loop extrusion where DNA is

reeled in from both regions outside of the loop. (B) Examples of non-symmetric loop extrusion events in interphase, showing one-sided reeling of DNA into the loop from only one region outside of the loop.

Figure 2- supplementary Figure 4: Characterization of loop movement and symmetry.

(A) Schematics of symmetric loop extrusion. Reeling in DNA from both sides at similar rates displaces the loop towards the shorter end of the DNA, as the smaller amount of slack in the shorter region is used up faster. (B) The displacement of a loop along the DNA strand by non-symmetric extrusion depends on the direction of extrusion. If the orientation of the extrusion machinery is random, it has equal chances to be directed towards the center of the DNA or the closest boundary. (C) We followed the movement of the DNA loop by tracking the relative location of the maximum of signal intensity for each time point. Top: kymograph of a metaphase looping event. Bottom: corresponding relative position of the loop for each time point. We then quantified the relative change in loop position along the DNA strand with respect to the centre of the DNA strand and the nearest boundary. This allowed us to plot the relative change in loop position over the corresponding symmetry score for all looping events in (D) metaphase and (E) interphase. We classified each looping event by its displacement towards the center, the nearest boundary, or as static, if the displacement did not exceed a threshold of 0.08 (see Methods). (F) Based on the displacement of all looping events, we could compare the probability for a loop to move to the centre of the DNA strand in metaphase and interphase.

Figure 2- supplementary Figure 5: Dependency of loop extrusion rate on extrusion symmetry and stall forces on initial relative DNA extension.

We quantified the loop extrusion rate as a function of extrusion symmetry (symmetry score) in both (A) interphase and (B) metaphase (C) for the events corresponding to Figure 2C. Using the worm-like chain model⁴¹, we computed the stall forces for both interphase and metaphase looping events from the plateau size of the loop and plot these values as a function of initial relative extension of the DNA strand before the loop formed. The hatched line shows the initial tension on the DNA strand before the onset of loop formation as a function of end-to-end distance of the DNA molecules. The resulting stall forces are conserved between inter- and metaphase and show a slight dependency on the initial relative extension of the DNA strand, possibly by selecting for stronger loops in stretched-out DNA molecules.

Figure 2- supplementary Figure 6: Dye-induced DNA lengthening.

(A) To correct for the concentration-dependent lengthening of DNA by intercalating dye Sytox Orange, we measured the extension (in μm) of DNA molecules that we hydrodynamically stretched using a buffer flow-rate corresponding to 1.54 pN, for all Sytox Orange concentrations employed in the study. The exponential fit to the data serves as a guide to the eye. (B) The corresponding contour lengths (cl) were determined for each dye concentration by applying the worm like chain model⁴¹ to the average measured DNA extension at the known stretching force of 1.54 pN.

Figure 3- supplementary Figure 1: Co-immunodepletions of *Xenopus* egg extracts using antibodies targeting H3-H4, cohesin, and condensin I and II.

(A) Co-immunodepletion of H3-H4 using anti-H4K12Ac antibodies and cohesin using anti-XRAD21 and anti-XSMC1 antibodies. H3 protein levels are detected using anti-H3 and exhibits a ~90-95% depletion of soluble H3-H4 heterodimers compared to IgG-depleted extract. XSMC1 protein levels are detected using anti-XSMC1, which exhibits a ~90% depletion. We used

anti-DM1a that detects tubulin as a loading control. (B) Co-immunodepletion of H3-H4 using anti-H4K12Ac antibodies and condensin using anti-XCAP-C and anti-XCAP-E antibodies. H3 protein levels are detected using anti-H3 and exhibits a ~90% depletion of soluble H3-H4 heterodimers compared to IgG-depleted extract. XCAP-C protein levels are detected using anti-XCAP-C, which displays a ~85% reduction, although the signal is rather weak and made it challenging to quantify. We used anti-DM1a that detects tubulin as a loading control. (C) Enzymatic depletion of ATP by apyrase (left) in H3H4-depleted interphase extract greatly reduces loop formation probability compared to control H3H4 depleted interphase extract (right).

Supplementary video captions

Video 1: Addition of crude *Xenopus* egg extract to a single strand of λ -phage DNA, visualized using Sytox Orange, leads to the generation of multiple highly-enriched DNA clusters, suggestive of nucleosomal formation along the strand.

Video 2: Addition of crude *Xenopus* egg extract to a single strand of λ -phage DNA, visualized using Sytox Orange, leads to the generation of multiple highly-enriched DNA clusters, suggestive of nucleosomal formation along the strand.

Video 3: Example of DNA loop formation in H3-H4-depleted egg extract arrested in metaphase visualized using Sytox Orange. The movie duration is 87 seconds and the scale bar is 5 μm .

Video 4: Example of DNA loop formation in H3-H4-depleted egg extract arrested in metaphase visualized using Sytox Orange. The movie duration is 90 seconds and the scale bar is 2 μm .

Video 5: Example of DNA loop formation in H3-H4-depleted egg extract in metaphase visualized using Sytox Orange. The movie duration is 195 seconds and the scale bar is 2 μm .

Video 6: Example of DNA loop formation in H3-H4-depleted egg extract in interphase visualized using Sytox Orange. The movie duration is 108 seconds and the scale bar is 2 μm .

Video 7: Example of DNA loop formation in H3-H4-depleted egg extract in interphase visualized using Sytox Orange. The movie duration is 80 seconds and the scale bar is 2 μm .

Video 8: Example of DNA loop formation in H3-H4-depleted egg extract in interphase visualized using Sytox Orange. The movie duration is 34 seconds and the scale bar is 2 μm .

Video 9: Example of hydrodynamically stretched DNA loops in H3-H4-depleted extract arrested in metaphase visualized using Sytox Orange. The movie duration is 19 seconds and the scale bar is 5 μm .

Video 10: Example of hydrodynamically stretched DNA loops in H3-H4-depleted extract

880 arrested in metaphase visualized using Sytox Orange. The movie duration is 16 seconds and
881 the scale bar is 5 μm .

882
883 **Video 11:** Example of a hydrodynamically stretched DNA loop in H3-H4-depleted interphase
884 extract visualized using Sytox Orange. The movie duration is 104 seconds and the scale bar
885 is 2 μm .

886
887 **Video 12:** Example of a hydrodynamically stretched DNA loop in H3-H4-depleted interphase
888 extract visualized using Sytox Orange. The movie duration is 4 seconds and the scale bar is
889 2 μm .

890
891 **Video 13:** Example of DNA loop formation in non-depleted crude extract visualized using
892 Sytox Orange. The movie duration is 87 seconds and the scale bar is 5 μm .

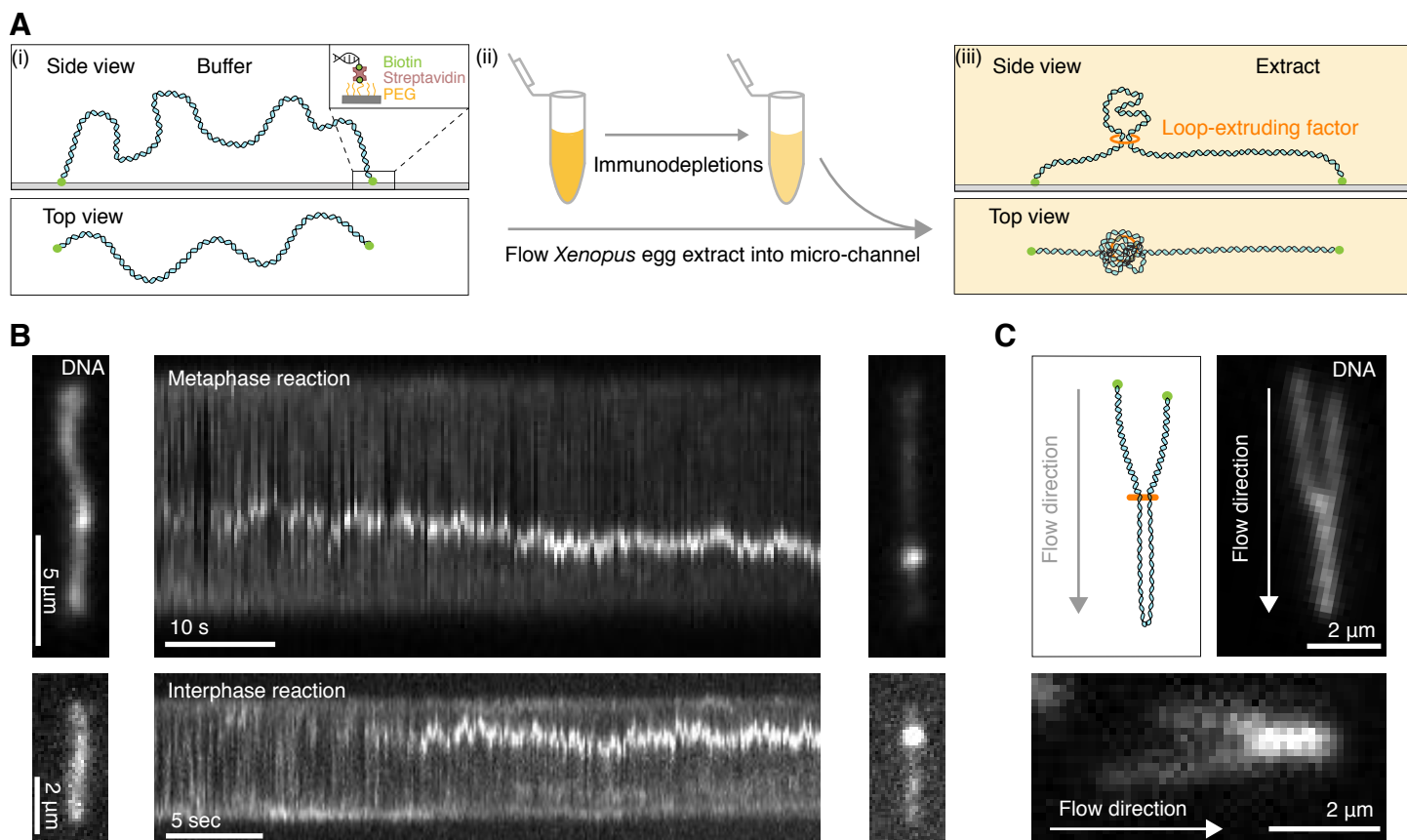


FIGURE 1 Golfier et al.

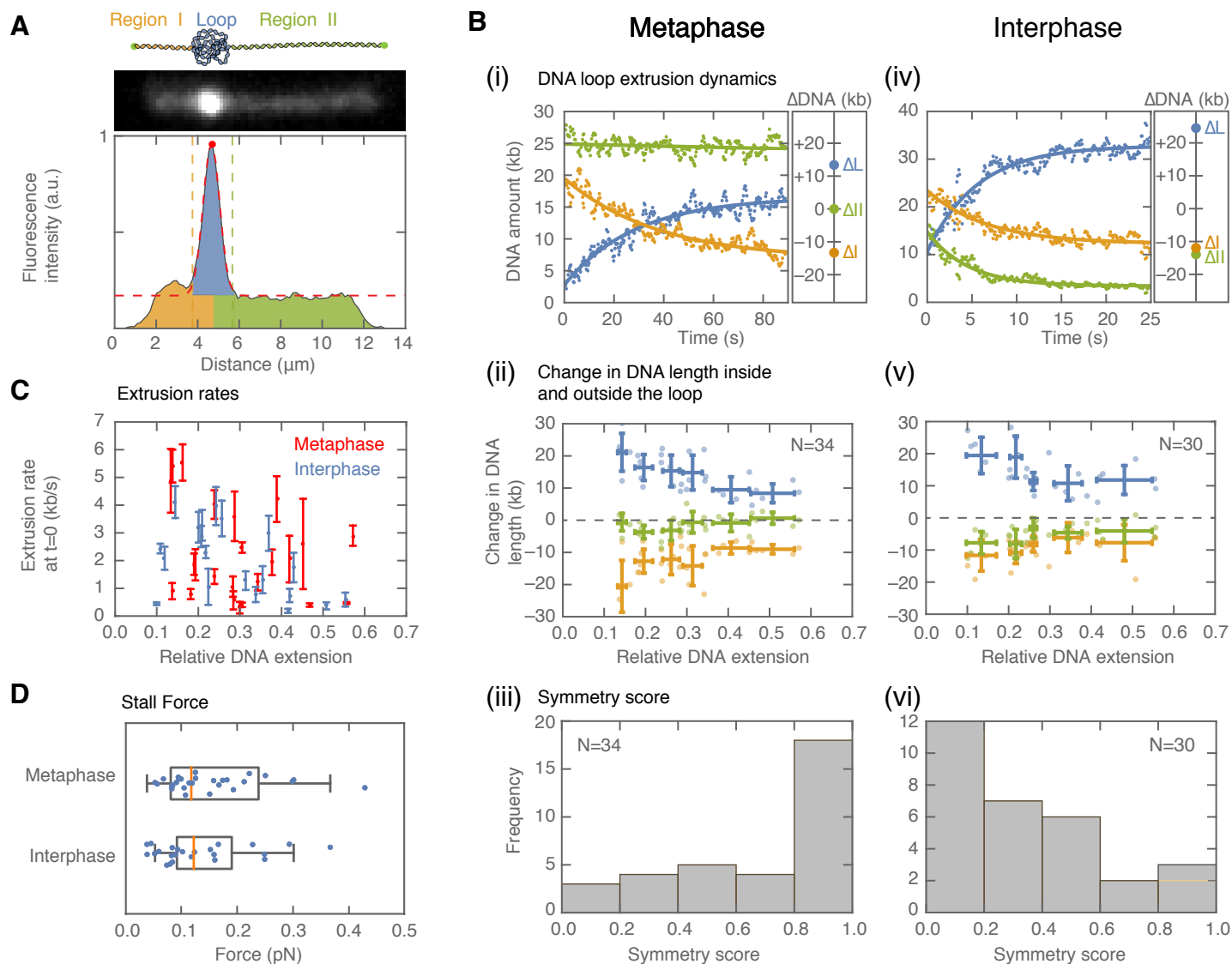


FIGURE 2 Golfier et al.

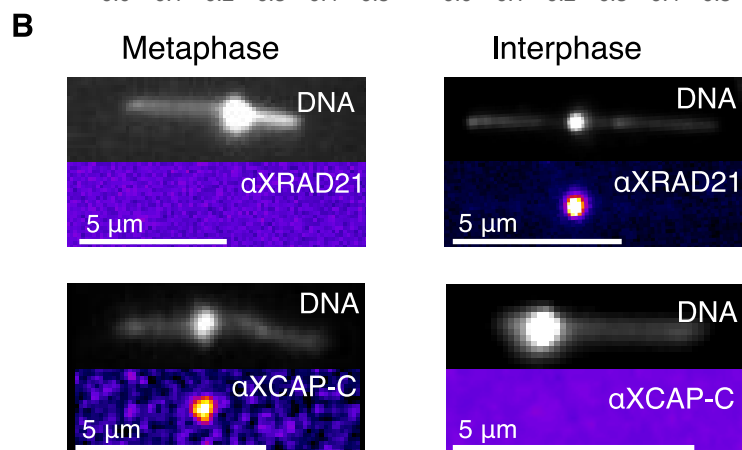
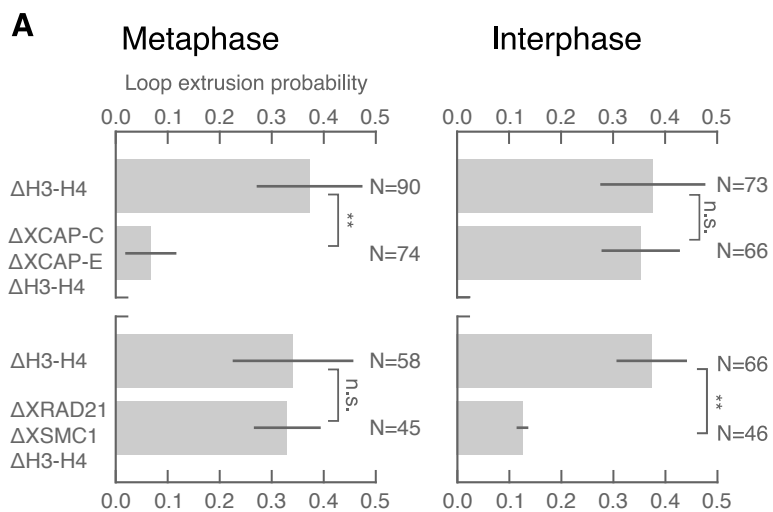


FIGURE 3 Golfier et al.

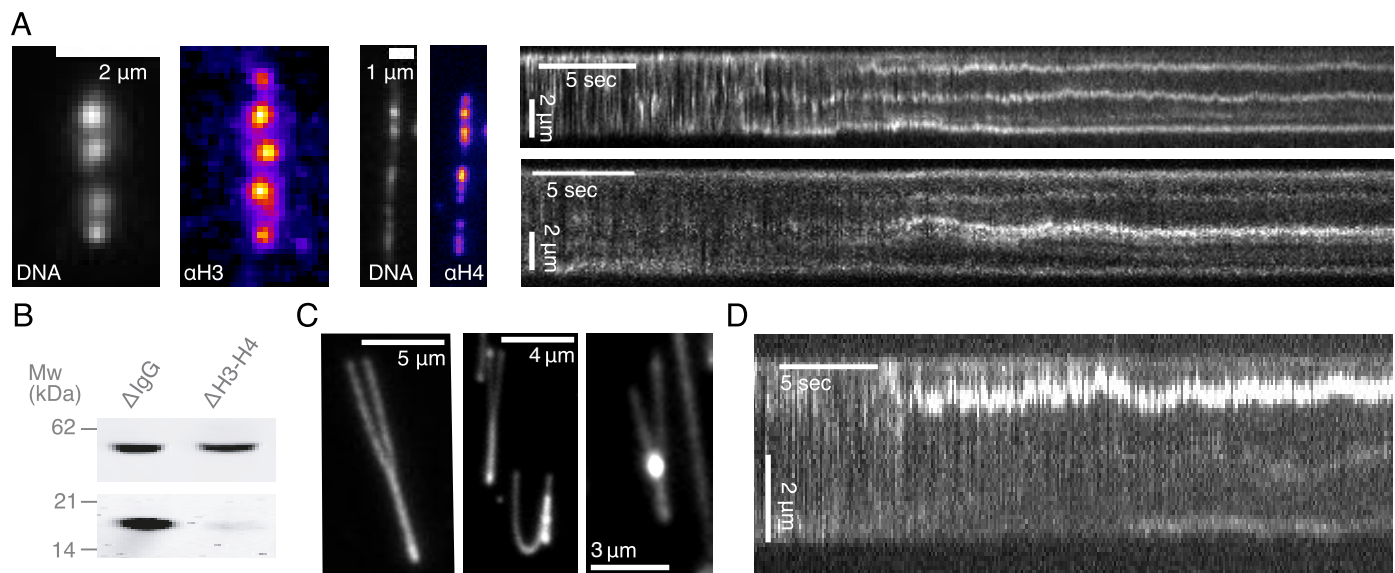


FIGURE 1 - FIGURE SUPPLEMENT 1 **Golfier et al.**

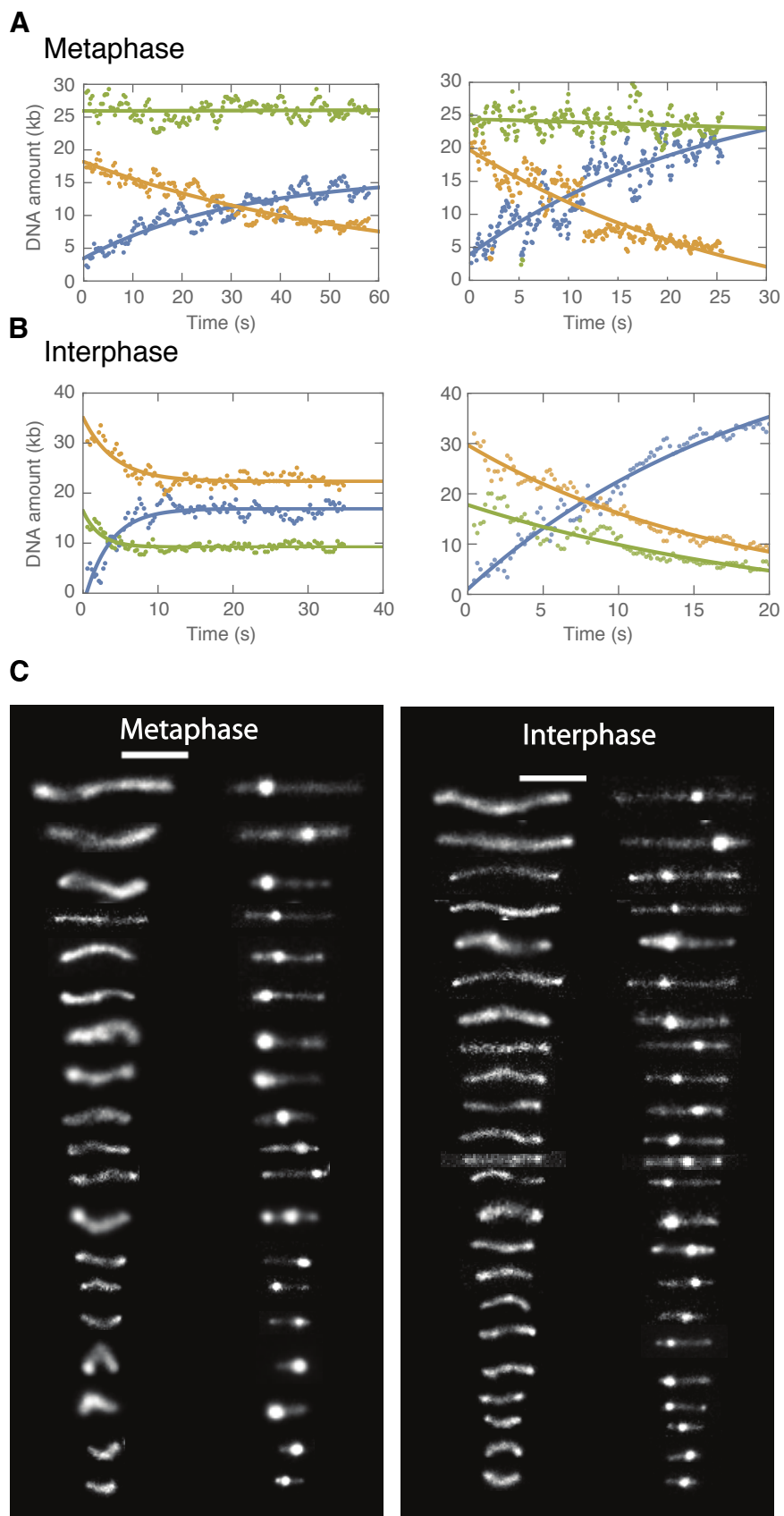


FIGURE 2 - FIGURE SUPPLEMENT 1 Golfier et al.

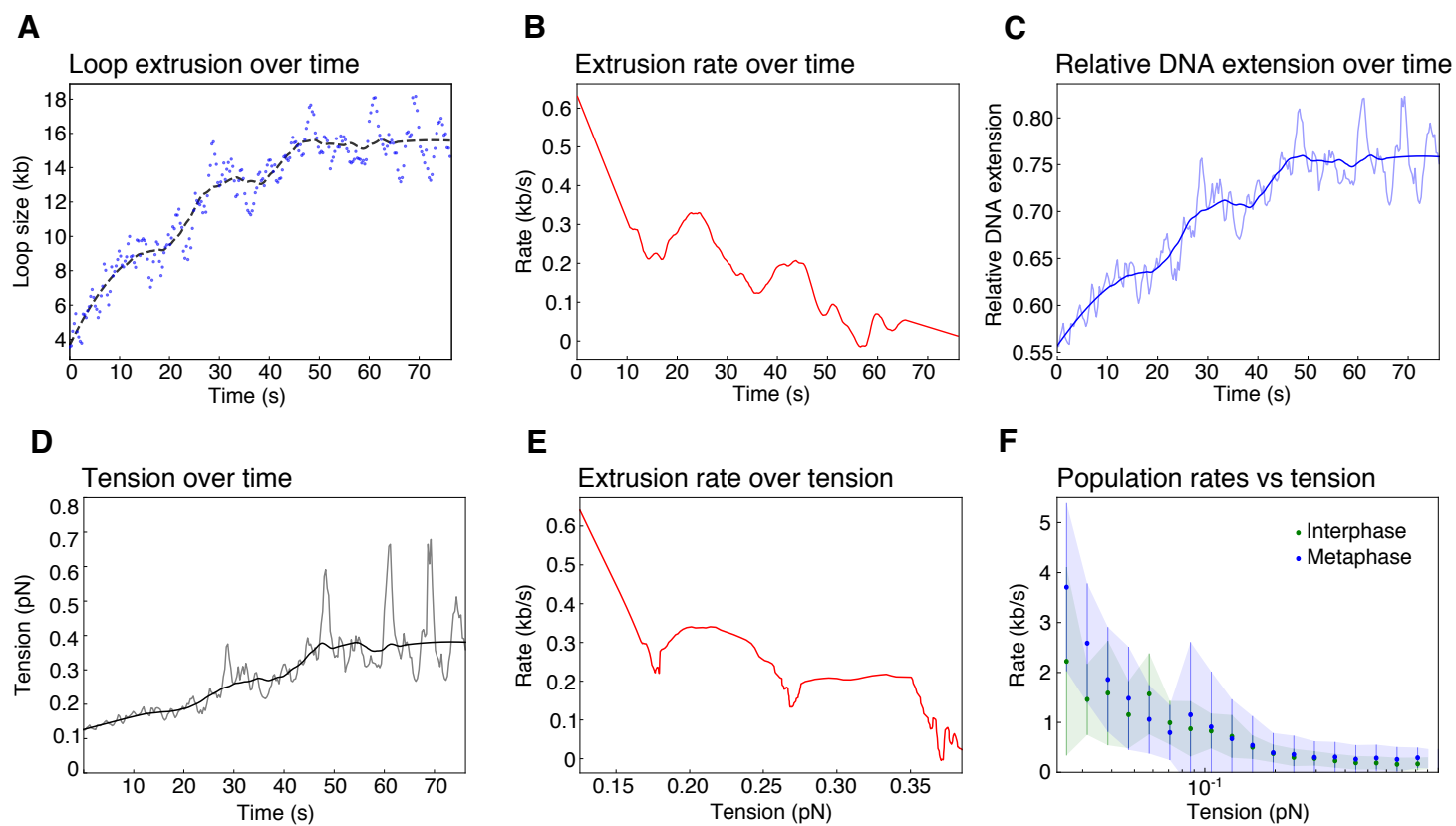
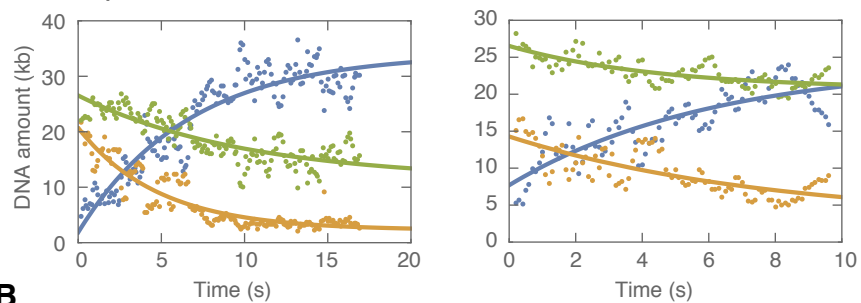
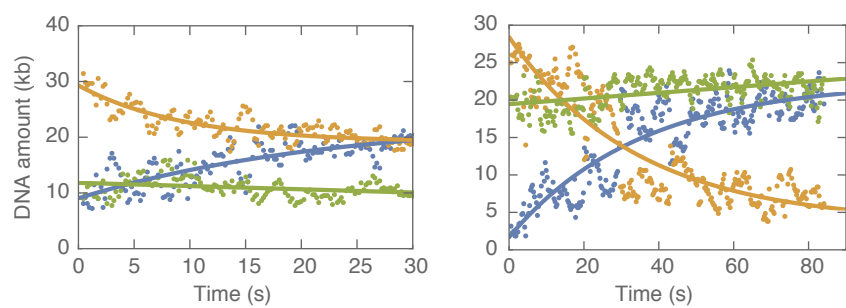


FIGURE S2 - FIGURE SUPPLEMENT 2 **Golfier et al.**

A**Metaphase****B****Interphase**

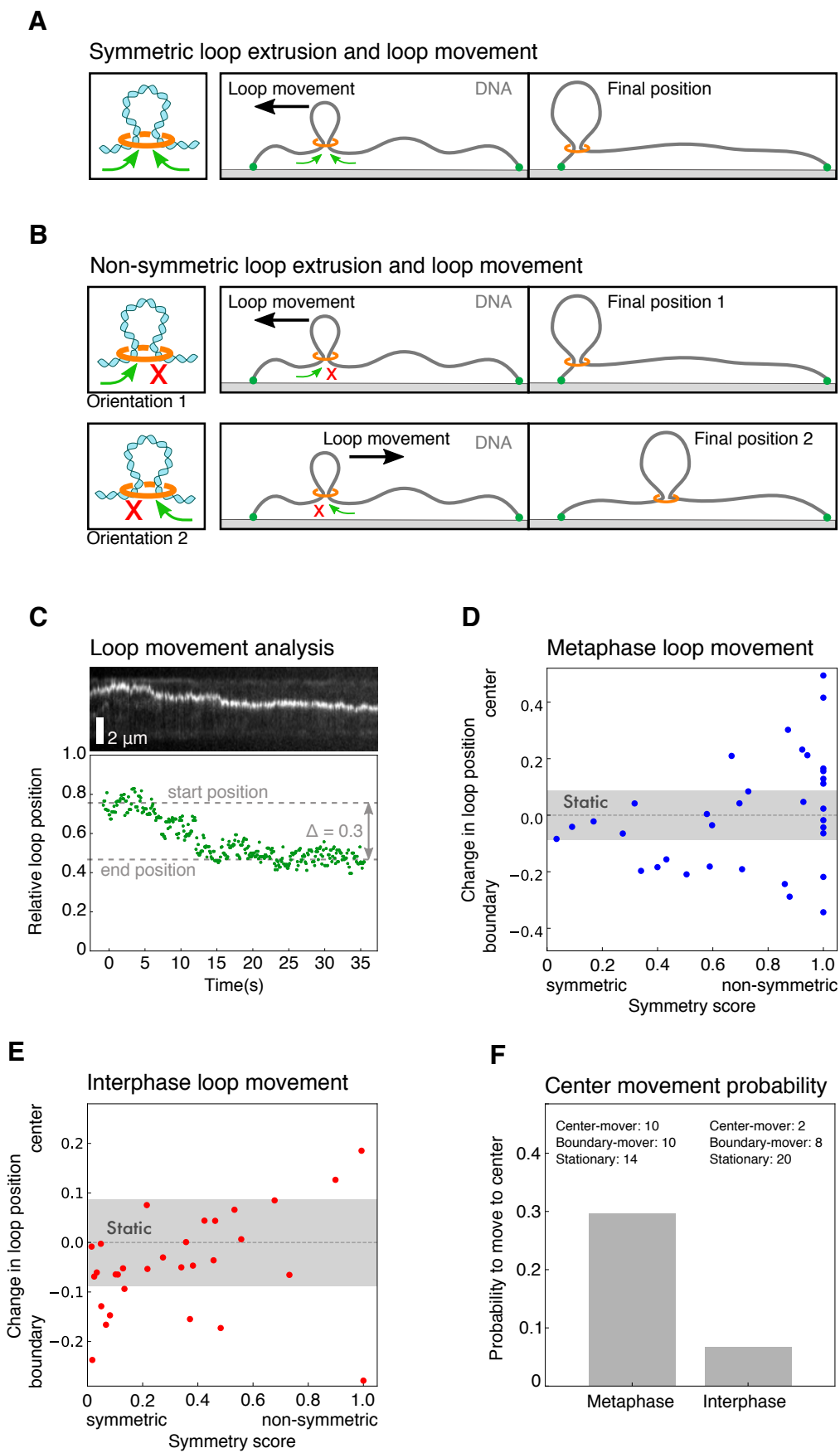


FIGURE 2 - FIGURE SUPPLEMENT 4 Golfier et al.

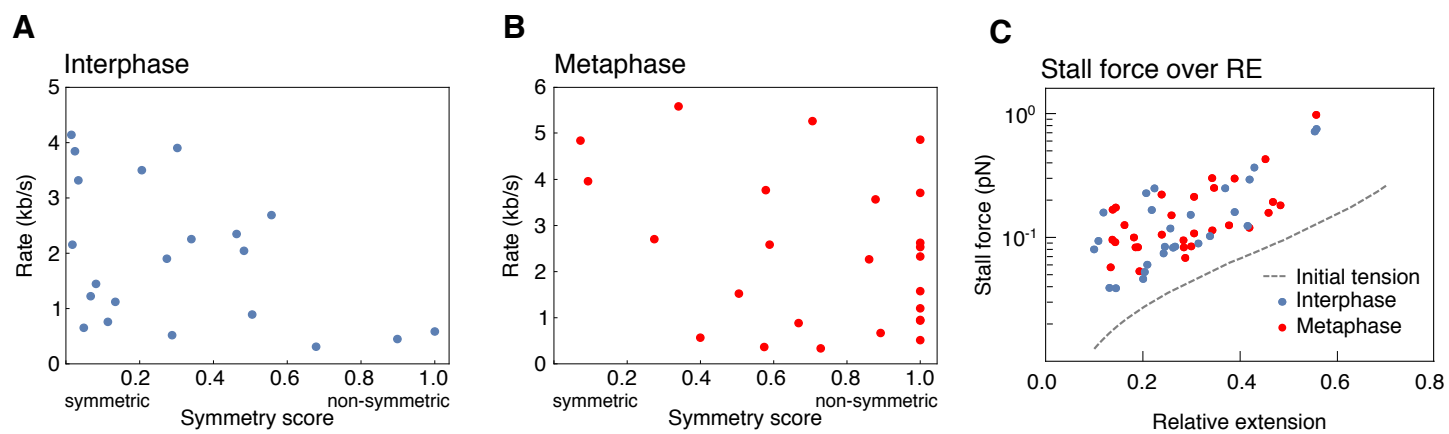


FIGURE 2 - FIGURE SUPPLEMENT 5 Golfier et al.

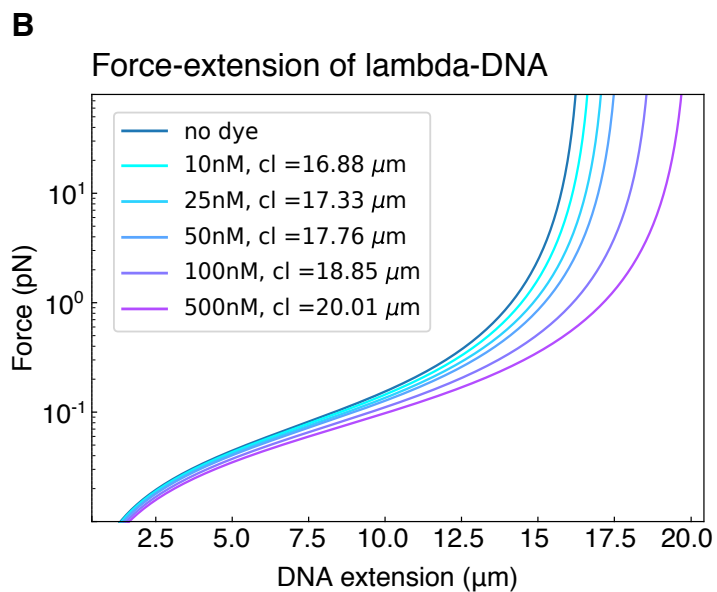
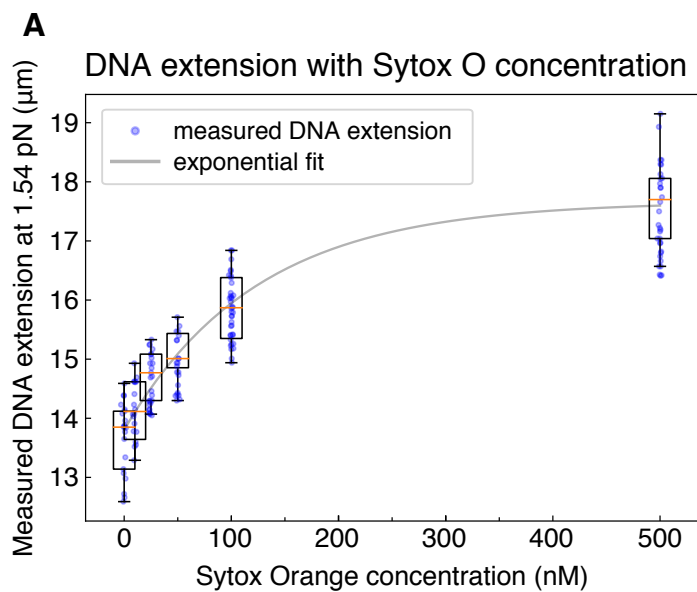


FIGURE 2 - FIGURE SUPPLEMENT 6 Golfier et al.

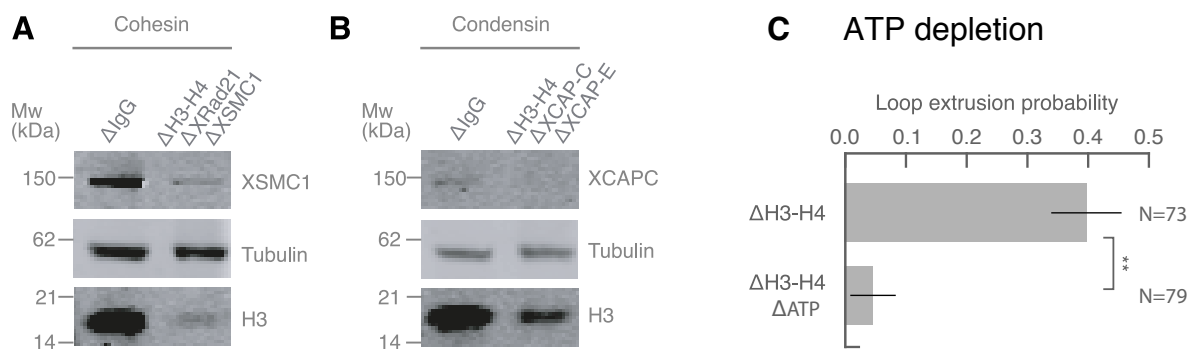


FIGURE 3 - FIGURE SUPPLEMENT 1 Golfier et al.